

Oxygen-Vacancies-Induced Enhancement in Photocatalytic Performance of Sea Urchin-Like $\text{Fe}_3\text{O}_4@\text{ZnO}$ Hollow Core–Shell Structures

Shuo Yang, Mengqu Pan, Jiayou Chen, Lili Wang, Chenzi Guo, Donglai Han,* and Lili Yang*

A novel sea urchin-like $\text{Fe}_3\text{O}_4@\text{ZnO}$ (S-FZ) hollow core–shell photocatalyst is developed, which achieves about fourfold higher photocatalytic degradation efficiency (84.4%) than the waxberry-type $\text{Fe}_3\text{O}_4@\text{ZnO}$ (W-FZ) photocatalyst due to its larger specific surface area. After postannealing at different temperatures under argon atmosphere, the photocatalytic degradation efficiency of S-FZ is effectively improved. When the annealing temperature is 500 °C, the degradation efficiency of S-FZ hollow core–shell structures is further improved to 99%, which is related to the synergistic effect of high density of oxygen vacancies. Such S-FZ catalysts are easily separated with a magnet and reused with only 2% loss in photocatalytic degradation efficiency after five circles. Herein, a practical approach toward high-efficient and recyclable photocatalysts is provided.

1. Introduction

Organic pollutants in water bodies, aggravated by human activities, are posing a serious threat to environment and human health.^[1,2] To solve this issue, various strategies, such as adsorption, coagulation, and membrane separation, have been explored.^[3,4] Compared with these traditional treatment methods, photocatalytic degradation of organic pollutants in water

has become a promising route due to its advantages of environmental friendliness, low energy consumption, high efficiency, and easy operation. Therefore, great deals of efforts have been devoted in recent years to improve the necessitating high efficiency, long-term stability, and low-cost semiconductor photocatalysts.^[5–8] So far, effective semiconductor photocatalysts mainly include ZnO ,^[9] TiO_2 ,^[10] Cu_2O ,^[4] ZnS ,^[11] CdS ,^[12] BiOX ($\text{X} = \text{Cl}, \text{Br}, \text{I}$),^[13,14] etc. Among various semiconductor materials, ZnO -based photocatalysis shows a promising future due to its attractive properties such as low cost, easy access, nontoxicity, high photosensitivity, high stability, a large piezoelectric constant, direct wide

bandgap, and tunable nanoscale size with adjustable optical and magneto-optical properties as well as perfect electron mobility ($205–300 \text{ cm}^2 \text{ V}^{-1} \text{ s}^{-1}$).^[4,5,15–20] Photocatalysis using ZnO has been widely used to remove many organic pollutants from aqueous solutions because ZnO is effective in producing hydroxyl radicals ($\cdot\text{OH}$) which can efficiently oxidize or mineralize organic compounds.^[21–23] However, the application of such photocatalysis to wastewater treatment is limited because of the difficulty in separating and recycling ZnO powder from the treated solutions. Traditional separation methods always cost too much and may result in secondary pollution caused by photocatalyst loss.^[24] Magnetic heterogeneous catalysts can provide a very efficient and convenient method for separating and recovering using external magnetic fields.^[25] So, combined ZnO with magnetic Fe_3O_4 nanoparticles (NPs), recyclable catalysts with great biocompatibility can be generated. Unfortunately, the performance of $\text{Fe}_3\text{O}_4@\text{ZnO}$ catalysts is largely hindered by their easy agglomeration. To solve this problem, improving the geometric structure of $\text{Fe}_3\text{O}_4@\text{ZnO}$ catalysts and exploring ways to further enhance photocatalytic performance have attracted enormous attention^[26,27] and become the focus of study.


So far, different morphologies of $\text{Fe}_3\text{O}_4@\text{ZnO}$ nanocomposites applied in the field of photocatalysis have been reported. For instance, Wang et al. reported that the $\text{Fe}_3\text{O}_4/\text{ZnO}$ nanocomposites which were composed of discoid-like and chip-like Fe_3O_4 NPs coated by ZnO nanorods exhibited higher photocatalytic efficiency ($\approx 76.5\%$) for RhB than ZnO (71.1%) within 180 min by UV irradiation.^[28] Wang et al. reported that 99.3% RhB in solution can be eliminated by $\text{Fe}_3\text{O}_4@\text{ZnO}$ core/shell NPs after

S. Yang, J. Chen, L. Wang
College of Science
Changchun University
Changchun 130022, China

M. Pan, L. Yang
College of Physics
Jilin Normal University
Siping 136000, China
E-mail: llyang1980@126.com, llyang@jlnu.edu.cn.

C. Guo
Chinese Academy of Sciences
Changchun Institute of Optics, Fine Mechanics and Physics
Changchun 130033, China

D. Han
School of Materials Science and Engineering
Changchun University of Science and Technology
Changchun 130022, China
E-mail: DLHan_1015@163.com, dlhan_1015@cust.edu.cn

 The ORCID identification number(s) for the author(s) of this article can be found under <https://doi.org/10.1002/pssa.202100421>.

DOI: 10.1002/pssa.202100421

60 min of UV irradiation, whereas ZnO only can eliminate 92.6% under the same condition.^[29] According to the work of Zhao et al., the photodegradation rate of Congo red by 3D Fe₃O₄/ZnO hierarchical structures was more than twice as fast as that by fusiform ZnO nanorods after 120 min.^[30] However, people only pay attention to the morphologies or assembly modes of the composites, but ignore the performance improvement of the materials themselves, which is the key to determining the photocatalytic performance of the composites. Therefore, it is very necessary to find a method to improve the performance of the composites themselves for enhancing the photocatalytic performance on the basis of constructing a special morphology.

In this work, we designed a novel sea urchin-like Fe₃O₄@ZnO (S-FZ) photocatalyst, that is, ZnO nanorods arrays were uniformly grown on Fe₃O₄ hollow spheres with the help of ZnO seeds layer to form a sea urchin-like hollow core-shell structure. On the one hand, the ZnO seeds interlayer can serve as an electronic barrier to block carrier transfer from ZnO to Fe₃O₄; on the other hand, the outer ZnO nanorod arrays work as photocatalysts to degrade pollutants. By applying such an S-FZ photocatalyst and a waxberry-type Fe₃O₄@ZnO (W-FZ) hollow core-shell catalyst in degrading rhodamine B (RhB), the S-FZ photocatalyst can achieve an efficiency as high as 84.4%, which is almost approximately fourfold higher than that of the W-FZ photocatalyst. Meanwhile, the photocatalytic degradation efficiency of S-FZ has been further effectively improved via postannealing treatment under argon atmosphere. When the annealing temperature was 500 °C, the degradation efficiency of S-FZ hollow core-shell structures was further improved to 99%, which was ascribed to the synergistic effect of high density of oxygen vacancies. The S-FZ photocatalysts could be easily separated with a magnet and their photocatalytic performance only decreases by 2% after five circles.

2. Results and Discussion

2.1. Morphology, Structure, and Properties of W-FZ and S-FZ Photocatalyst

Figure 1 shows the XRD patterns of Fe₃O₄ hollow spheres, W-FZ, and S-FZ core-shell structures. All diffraction peaks of Fe₃O₄ hollow spheres are in accordance with the phase structure of pure face-centered cubic Fe₃O₄ (JCPDS no. 19-0629).^[31] As shown in Figure 1b,c, the diffraction peaks of the as-synthesized W-FZ and S-FZ core-shell structures located at 30.0, 35.5, 43.1, 53.4, 57.0, and 62.7° (marked by octothorpe) match with the (220), (311), (400), (422), (511), and (440) planes of face-centered cubic Fe₃O₄ (JCPDS no. 19-0629).^[31] Meanwhile, the diffraction peaks at 31.7, 34.3, 36.2, 47.4, 56.5, and 62.7° (marked by asterisk) can be indexed to (100), (002), (101), (102), (110), and (103) planes of hexagonal wurtzite ZnO (space group *p63mc*, JCPDS card no.36-1451).^[32] No other peaks are observed, indicating that the Fe₃O₄@ZnO nanocomposites are synthesized.

The field emission scanning electron microscope (FESEM) images are shown in Figure 2 to check the morphology evolution of Fe₃O₄, ZnO, W-FZ, and S-FZ structures. As shown in Figure 2a, d, the Fe₃O₄ hollow spheres are approximately monodispersed with a mean diameter of ≈700 nm; the rough surfaces are

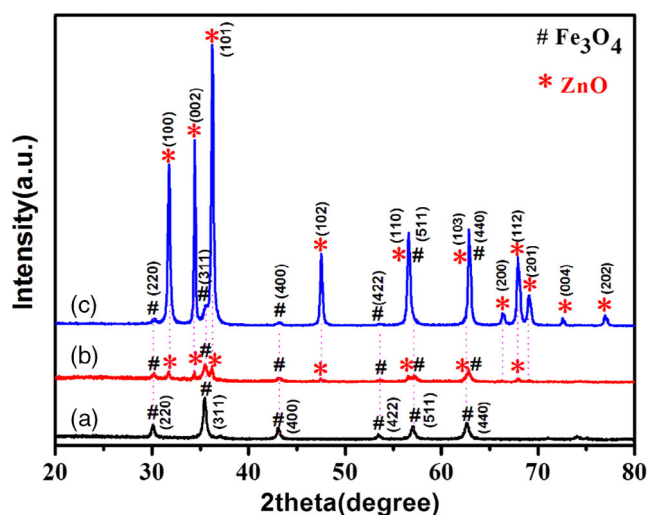


Figure 1. XRD patterns of a) Fe₃O₄ hollow spheres, b) W-FZ structure, and c) S-FZ structure.

beneficial for further shell coating. After sonochemical deposition, the samples grow larger and evolve into “waxberry” shape, as shown in Figure 2b,e, proving that a large amount of ZnO NPs have been immobilized onto the Fe₃O₄ spheres. As shown in Figure 2c,f, the sea urchin-type S-FZ structures have been obtained by an improved two-step self-assembly hydrothermal method, that is, the ZnO nanorods with average length of 450 nm are uniformly grown on the surface of Fe₃O₄ spheres to form a sea urchin-like 3D structure, which helps create a large specific surface area.

The TEM and x-ray energy dispersive spectrometer (EDS) elemental mapping tests were conducted to further verify the morphology and configuration of the Fe₃O₄, W-FZ, and S-FZ structures and reveal their chemical element composition. Figure 3a shows the TEM image of Fe₃O₄ sphere. Obviously, the edge of the Fe₃O₄ sphere is much darker than its center, which provides strong evidence for the formation of hollow structures. The average diameter of these hollow spheres is about 630 nm and the shell thickness is about 150 nm. Figure 3b also shows a distinguishable core-shell structure, in which the cloud-like shell resembles a waxberry with an approximate thickness of 70–100 nm. Figure 3c shows a “sea urchin”-like structure, which is in good agreement with earlier SEM results. Figure 3e–g and Figure 3i–k shows the EDS elemental mapping of Fe, O, and Zn atoms of W-FZ and S-FZ structures, respectively. Clearly, Fe, O, and Zn atoms are uniformly dispersed in both samples. Moreover, the Fe element is concentrated at the core zone, whereas the O and Zn elements are evenly distributed in the entire nanocomposites, which confirms the formation of core-shell structures.

Figure 4a shows the room-temperature PL spectra of the W-FZ (red line) and S-FZ (black line) structures. The PL spectrum of S-FZ structure consists of two emission bands, a sharp UV emission peak centered at 380 nm and a broad visible emission (VE) band at 450–700 nm. The sharp UV emission band originates from the recombination of free excitons^[33,34] and the broad VE is attributed to intrinsic defects such as oxygen vacancies and zinc vacancies in ZnO.^[35–37] In comparison, no sharp UV emission peak can be observed in the PL spectrum of W-FZ structure at all, only a strong VE band appears. The possible

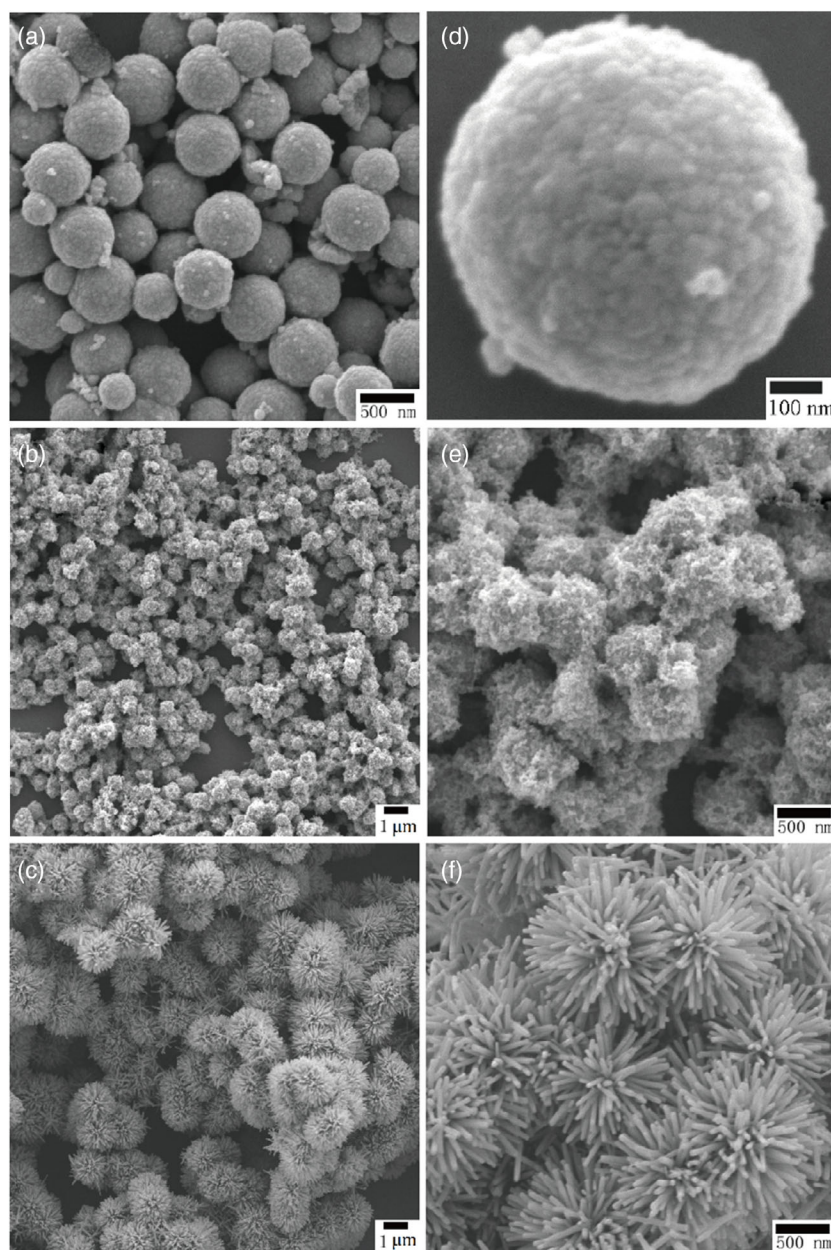


Figure 2. FESEM images of as-prepared samples: a,d) Fe_3O_4 hollow spheres, b,e) W-FZ, and c,f) S-FZ.

explanation can be described as follows: as for the W-FZ structure, the Fe^{3+} ions in Fe_3O_4 act as photogenerated electron-trapping sites,^[38,39] and the interaction between the ZnO NPs and Fe_3O_4 spheres would lead to charge energy transfer from the ZnO NPs to the Fe_3O_4 spheres, which hence reduces the intensity of UV emission. Meanwhile, as shown in XRD patterns, the crystal quality of W-FZ structures is much worse than that of S-FZ structures. Therefore, only a weaker broad VE band can be observed. In contrast, as for S-FZ structures, the ZnO NPs are first deposited on the surface of Fe_3O_4 hollow spheres to form a seed layer before growing the ZnO nanorods. We can infer this introduced ZnO seed layer as a kind of carrier barrier,^[40,41] which

will inhibit the migration of photon-generated carriers from the shell to the core and finally result in the stronger UV emission, indicating that more photogenerated carriers can take part in the photocatalytic process.

To investigate the magnetic property of these samples, magnetic hysteresis (M–H) loops of Fe_3O_4 hollow spheres, W-FZ, and S-FZ structures at room temperature are shown in Figure 4b. All samples show superparamagnetic properties considering that no obvious remanence or coercivity is observed from the M–H loops. The Fe_3O_4 hollow spheres have a maximum magnetization saturation (M_s) value of 89 emu g^{-1} , which is very close to their bulk value (92 emu g^{-1}).^[42] After coating

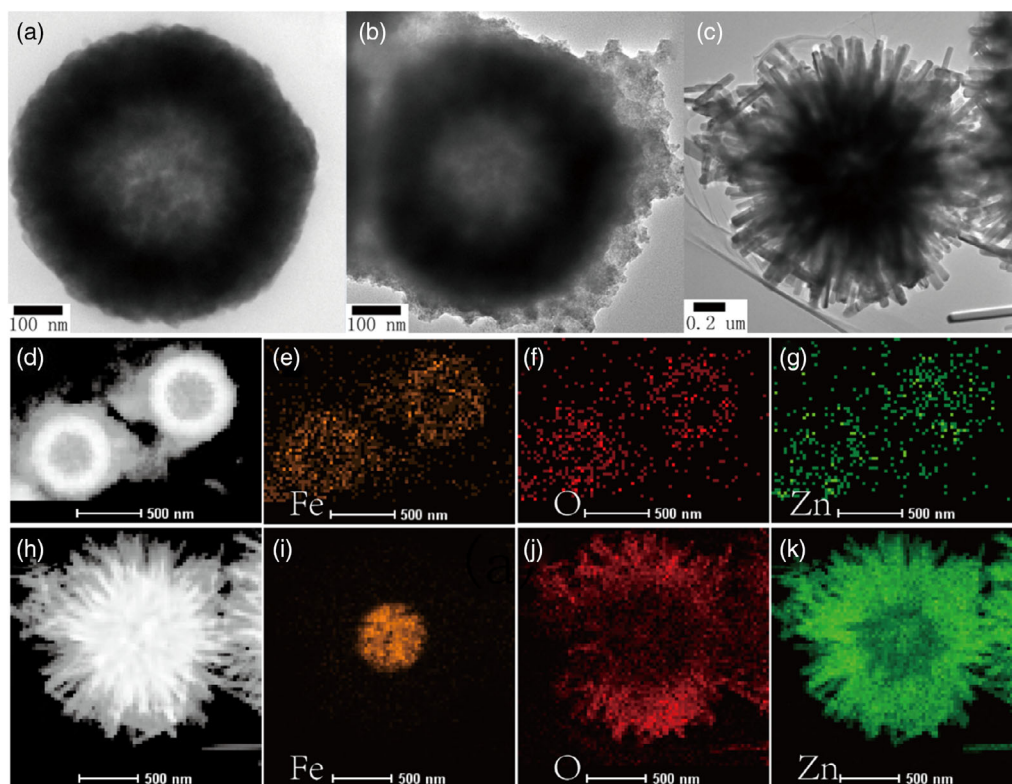


Figure 3. TEM images of as-prepared samples: a) Fe₃O₄ hollow spheres, b) W-FZ, and c) S-FZ structures. The EDS elemental mappings of d–g) W-FZ and h–k) S-FZ structures.

with ZnO, the M_s value of W-FZ and S-FZ structures decreases to 59 and 8.5 emu g^{−1}, respectively, which can be easily understood concerning the decrease in Fe₃O₄ proportion in the Fe₃O₄@ZnO nanocomposites. Nonetheless, the W-FZ and S-FZ core-shell structures still exhibit good magnetic properties.

The photocatalytic performances of the W-FZ and the S-FZ structures are evaluated by degrading RhB under UV irradiation. It is shown in Figure 4c,d that the absorption peak intensity of RhB at ≈550 nm decreases with time, which indicates that the RhB molecules can be degraded by both W-FZ and S-FZ structures under UV irradiation. As shown in Figure 4e, the photocatalytic degradation efficiency of W-FZ is only ≈17.8%, whereas the degradation efficiency of S-FZ is ≈84.4% after 8 h UV irradiation.^[43,44] The enhancement of S-FZ photocatalytic performance can be ascribed to the synergy of the following two factors: its special 3D structure with a larger specific surface area increases the photocatalytic sites for degradation RhB and allows scattering of the incident light to achieve multiple absorption and the ZnO seed layer can block the photon-generated carriers transfer from ZnO nanorods to Fe₃O₄ hollow spheres, which can provide more carriers to take part in the photocatalytic process.

2.2. Annealing Effect on the Photocatalytic Property of S-FZ Photocatalyst

To further improve the photocatalytic performance of as-synthesized S-FZ photocatalysts, postannealing treatments

were conducted for 3.5 h in air and Ar atmosphere, respectively, after the calciner was preheated to 300, 400, and 500 °C respectively. The S-FZ photocatalysts after postannealing treatments are then applied to degrade RhB under UV irradiation. As shown in Figure 5a,b, the degradation efficiency of the S-FZ annealed at 300, 400, and 500 °C is 83.3, 93.7, 95.2% (in air) and 90.1, 96.5, and 99.0% (in argon), respectively. Compared with the results in Figure 4, we can see that the photocatalytic efficiency of S-FZ is greatly improved after postannealing treatment under both air and Ar atmosphere. Post annealing under Ar atmosphere exhibits better performance than that of air atmosphere at each annealing temperature point. Meanwhile, the velocity of photocatalytic efficiency via the annealing temperature of S-FZ annealed under Ar atmosphere is faster than under air atmosphere. Finally, the S-FZ annealed under Ar atmosphere at 500 °C achieves the best performance.

To unveil the related mechanism of enhanced photocatalytic activity, the XRD patterns and SEM images of the S-FZ samples after postannealing treatment at different temperatures and atmospheres are shown in Figure S1 and S2, Supporting Information. We can see that the crystal structures and morphologies of S-FZ samples are hardly affected by the postannealing treatment. However, when the annealing temperature is 500 °C, the intensities of diffraction peaks in XRD patterns of the one annealed under air or Ar atmospheres turn weaker than that of the as-synthesized S-FZ sample, indicating that their crystal qualities turn poor. It might be related to the improved photocatalytic activity.

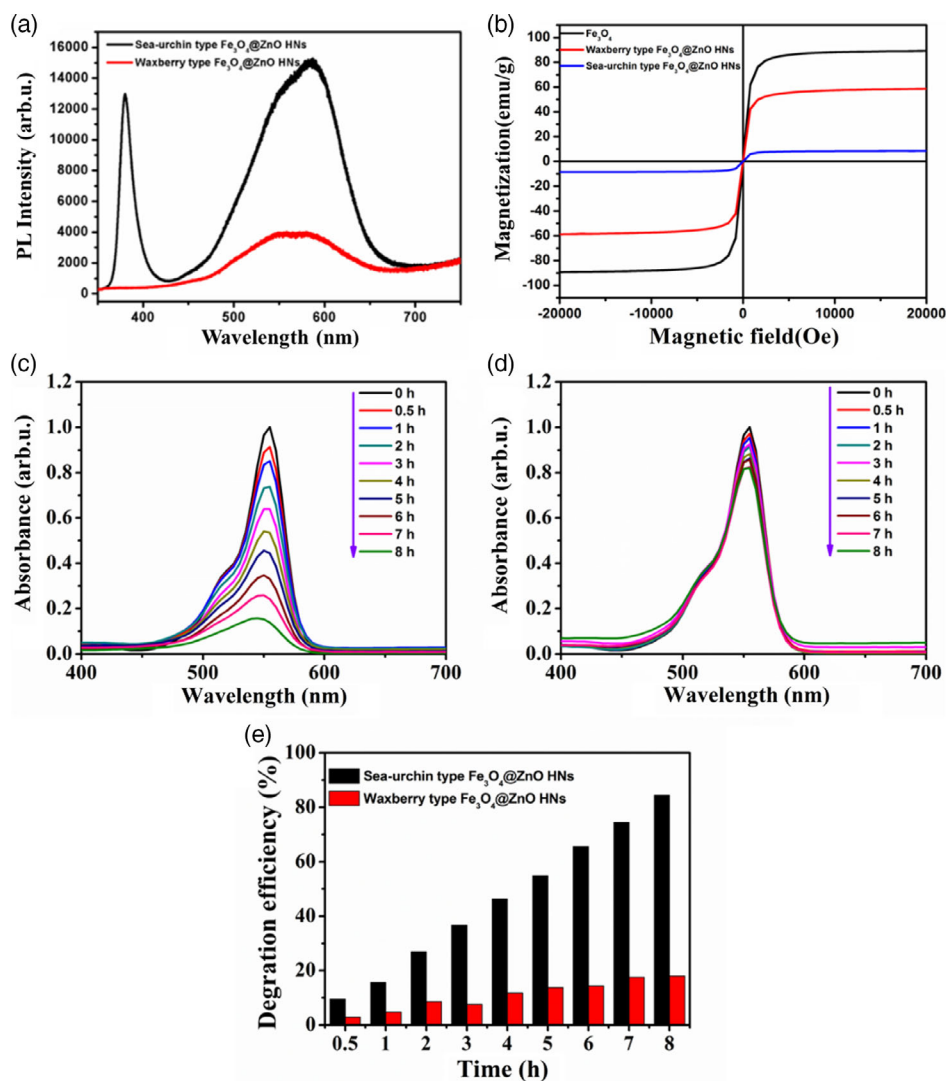


Figure 4. a) Room-temperature PL spectra of W-FZ (red line) and S-FZ (black line) structures. b) Magnetic hysteresis loops of Fe₃O₄ hollow spheres, W-FZ, and S-FZ structures. UV absorption spectra of RhB after being degraded for different times by c) W-FZ and d) S-FZ. e) Degradation efficiency versus reaction time for W-FZ (red bar) and S-FZ (black bar).

To prove the earlier deduction, the normalized room-temperature PL spectra of S-FZ annealed at different temperatures and atmospheres are shown in Figure 5c,d, which are similar to the spectrum of as-synthesized S-FZ discussed earlier and previous reports about ZnO PL spectra.^[45–48] After annealing at different temperatures and atmospheres, the intensity of visible band emission is obviously enhanced in comparison with that of as-synthesized S-FZ structures, which proves that more intrinsic defects are generated in ZnO nanorods after postannealing treatment, exhibiting good consistency with the above XRD results.

To find out the relationship between defect variation and the corresponding catalytic performance via postannealing treatment, Gaussian fitting for the PL spectra of S-FZ annealed at different temperatures and atmospheres is conducted within the visible range from 450 to 750 nm as it originates from intrinsic defects. As shown in Figure 6, all peaks of S-FZ annealed at 300, 400, or 500 °C (in air or argon atmosphere) can be divided into two

Gaussian symmetry peaks centered at 540 and 602 nm, respectively. In other words, two types of intrinsic defects exist in the S-FZ samples. As reported,^[30,31] the green emission peak (GP) at 540 nm is related to oxygen vacancy and the orange emission peak (OP) centered at 602 nm is ascribed to the oxygen interstitial.^[49,50] The intensity ratio of GP to OP (I_{GP}/I_{OP}) via annealing temperature and atmosphere is shown in Figure 8b. As shown in Figure 8b, the I_{GP}/I_{OP} of the as-synthesized S-FZ is 0.92. As the temperature increases from 300 to 500 °C in air atmosphere, the I_{GP}/I_{OP} value increases from 1.80 to 3.69. The I_{GP}/I_{OP} value can be further increased by annealing in Ar atmosphere.^[51–54] Therefore, we can conclude that more oxygen vacancies can be generated in Ar atmosphere and high temperature. Such variation tendency in I_{GP}/I_{OP} is very consistent with that of enhanced velocity of photocatalytic efficiency discussed earlier, indicating that oxygen vacancies play a great role in improving the photocatalytic activity of S-FZ. According to previous reports, these oxygen vacancies can

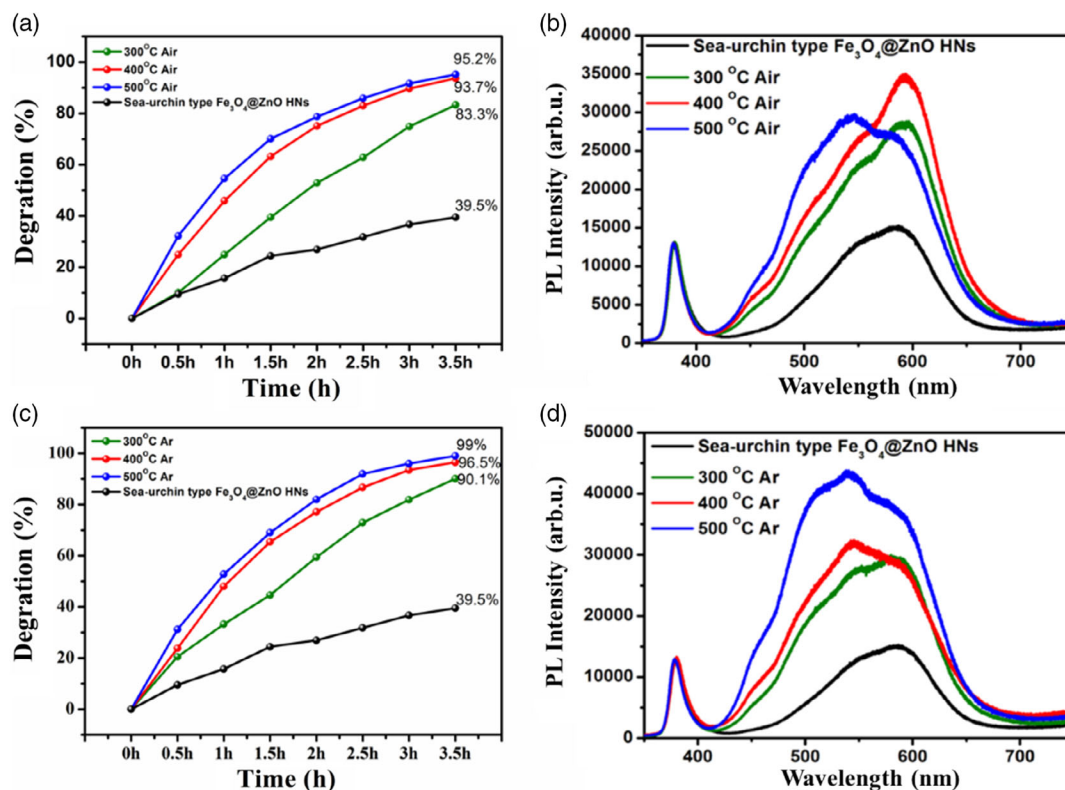


Figure 5. a,b) Photodegradation efficiency of RhB as a function of irradiation time by S-FZ structures annealed at different temperatures and atmospheres. c,d) Normalized PL spectra of S-FZ structures annealed at different temperatures and atmospheres.

serve as trapping centers and hinder the recombination of photogenerated electron-hole pairs and facilitate the separation of photogenerated carriers, which finally improves the photocatalytic activity of materials.^[55]

Figure 7a shows the M-H loops of the treated S-FZ catalysts annealed at different temperatures under Ar atmosphere. All samples exhibit superparamagnetism. Although the saturation magnetization is weakened with the increase in annealing temperature, it is still good enough for magnetic separation. To prove it, we further investigate the photostability and reusability of the S-FZ annealed at 500 °C under Ar atmosphere. After a magnet collection and a simple step of water washing, the S-FZ catalysts can be reused with only 2% decrease in degradation efficiency after five cycles, as shown in Figure 7b. It indicates that our S-FZ catalysts possess an excellent photostability and recyclability throughout the photocatalytic process.

2.3. Photocatalytic Mechanism of Postannealed S-FZ Photocatalyst

To explain the enhanced photocatalytic performance of our S-FZ photocatalyst, we further investigated the possible mechanisms. First, the unique 3D hierarchical structure of our S-FZ photocatalyst not only has a larger specific surface area to provide more photocatalytic sites, but also allows scattering of the incident light and multiple absorption,^[56,57] which can enhance the utilization of light, as shown in Figure 8a. Second, the postannealing

process increased the concentration of oxygen species. As shown in Figure 8b, the oxygen species (such as O_2^- and OH^-) derived during the photocatalytic degradation process could be easily captured by these oxygen vacancies and transformed into $\cdot\text{O}_2^-$ and $\cdot\text{OH}$, so that the photocatalysis process is accelerated, preventing the recombination of photogenerated electron-hole pairs and finally leading to the enhanced photocatalytic activity.^[30]

3. Conclusion

In this work, we develop a novel S-FZ hollow core-shell photocatalyst via an improved self-assembly hydrothermal method. The unique 3D hierarchical structure of our S-FZ photocatalyst possesses almost approximately fourfold higher photocatalytic degradation efficiency than that of the W-FZ photocatalyst as it not only owns a larger specific surface area to provide more photocatalytic sites, but also allows scattering of the incident light to enhance the utilization of light. The design of ZnO seed layer for S-FZ structures serves as an electronic barrier to block the photon-generated carrier transfer from ZnO nanorods to Fe_3O_4 hollow spheres. More importantly, postannealing treatment is introduced to control the intrinsic defects within the ZnO nanorods, and the photocatalytic degradation efficiency of S-FZ annealed at 500 °C under Ar atmosphere is further improved to 99% due to the increased oxygen vacancies, which also exhibits excellent reusability. This work provides a practical approach toward high-efficient and recyclable photocatalysts.

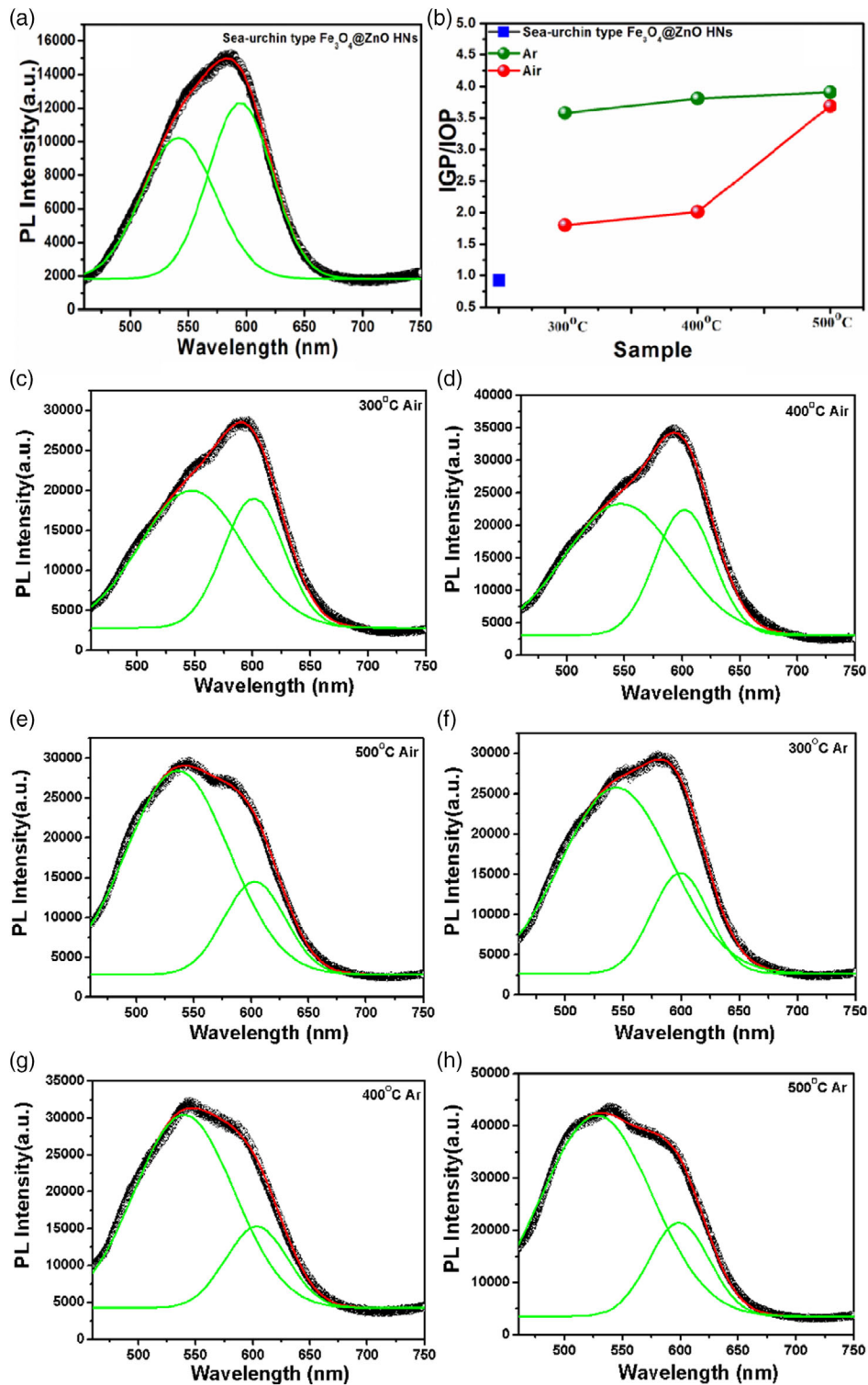


Figure 6. Gaussian fitting results of the VE band in the range of 450–750 nm of S-FZ annealed at different temperatures and atmospheres a) untreated at c–e) 300, 400, 500 °C in air atmosphere and at f–h) 300, 400, 500 °C in argon atmosphere. b) I_{GP}/I_{OP} plot via annealing temperature and atmosphere. The original profiles are shown in black, the Gaussian fits are overlaid in red, and the fitted peaks are shown with green lines.

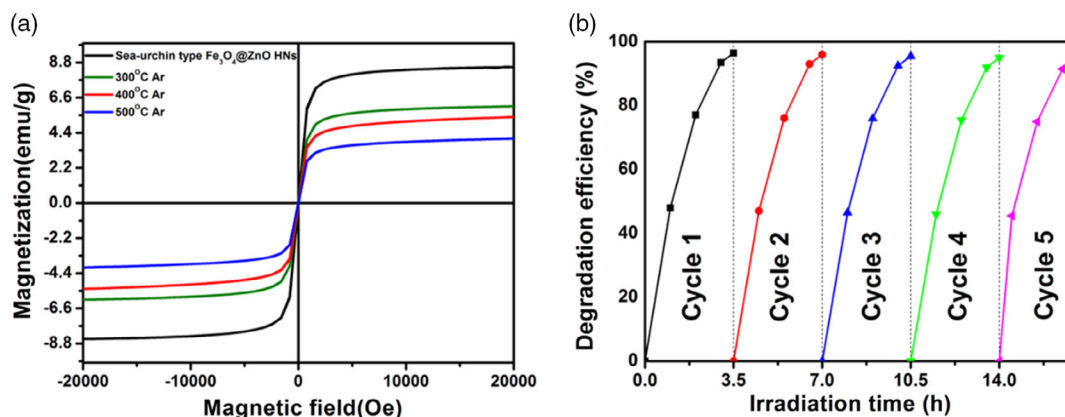


Figure 7. a) Room-temperature (300 K) magnetic hysteresis loops of the S-FZ annealed at 300, 400, and 500 °C in argon atmosphere. b) The reusability of the S-FZ annealed at 500 °C in argon atmosphere for RhB decoloration.

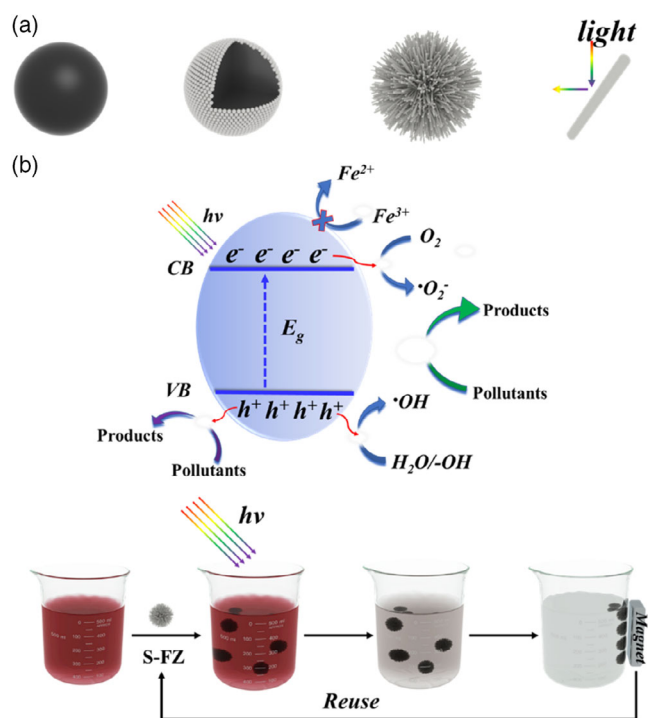


Figure 8. a) Schematic illustration of multiabsorption within S-FZ. b) Possible photocatalytic mechanism of the S-FZ photocatalyst.

4. Experimental Section

Materials: Ferric chloride hexahydrate ($\text{FeCl}_3 \cdot 6\text{H}_2\text{O}$), sodium acetate trihydrate ($\text{NaAc} \cdot 3\text{H}_2\text{O}$), sodium dodecylsulfate (SDS), ethylene glycol (EG), sodium hydroxide (NaOH), zinc acetate dihydrate ($\text{Zn}(\text{Ac})_2 \cdot 2\text{H}_2\text{O}$), polyvinylpyrrolidone (PVP), zinc nitrate hexahydrate ($\text{Zn}(\text{NO}_3)_2 \cdot 6\text{H}_2\text{O}$), hexamethylenetetramine (HMTA), deionized water, ethylalcohol ($\text{C}_2\text{H}_5\text{OH}$), and rhodamine B (RhB) were in analytical grade without further purification.

Synthesis of Fe_3O_4 Hollow Spheres: Fe_3O_4 magnetite hollow spheres were prepared by the solvothermal method. First, 1.62 g of $\text{FeCl}_3 \cdot 6\text{H}_2\text{O}$ was dissolved in 60 mL of ethylene glycol (EG) under vigorous stirring for 0.5 h. Then, 2.7 g of $\text{NaAc} \cdot 3\text{H}_2\text{O}$ was added into the obtained clear yellow solution and stirred for 1 h. After that, 0.6 mmol sodium dodecyl sulfate (SDS) was added and stirred for another 1 h. The mixture was later

transferred into a 100 mL Teflon-lined stainless-steel autoclave and maintained at 200 °C for 12 h. After the reaction, the autoclave was cooled down to room temperature naturally. With the help of a magnet, the black magnetite particles were collected and then repeatedly washed with ethanol and deionized water six times. Finally, the washed particles were dried in a vacuum oven at 60 °C for 12 h and stored in a dryer.

Synthesis of W-FZ Hollow Core-Shell Structures: The W-FZ structures were synthesized by an improved sonochemical deposition approach. First, 10 mg of the as-prepared Fe_3O_4 hollow spheres was dispersed in 160 mL of ethanol solution containing 0.27 g $\text{Zn}(\text{Ac})_2 \cdot 2\text{H}_2\text{O}$. The mixture was treated with ultrasonics at 60 °C for 1.5 h. Then, 65 mL ethanol solution containing 0.15 g NaOH was added into it. After that, the solution was treated under ultrasonics for 0.5 h with mechanical stirring at 60 °C for 3 h. Finally, the W-FZ hollow core-shell structures were collected by a magnet, followed by repeatedly washing with ethanol and deionized water six times. The obtained products were dried in a vacuum oven at 60 °C for 6 h and stored in a dryer.

Synthesis of the S-FZ Hollow Core-Shell Structures: The S-FZ structures were prepared by an improved two-step self-assembly hydrothermal method. 1) First, ZnO seed layer was covered on the Fe_3O_4 hollow spheres. After adding 65 mL ethanol and 0.15 g NaOH into another 160 mL ethanol solution containing 0.27 g $\text{Zn}(\text{Ac})_2 \cdot 2\text{H}_2\text{O}$, 0.375 g PVP, and 50 mg as-prepared Fe_3O_4 , the ZnO seeds were grown on the surface of Fe_3O_4 hollow spheres. The reaction took 1.5 h under stirring and ultrasonic treatment at 60 °C. 2) Second, 0.1 M $\text{Zn}(\text{NO}_3)_2 \cdot 6\text{H}_2\text{O}$ solution and 0.1 M hexamethylenetetramine (HMTA) solution were mixed together. The seeded Fe_3O_4 hollow spheres obtained in the above step were added into the mixture under mechanical stirring at 80 °C for 4 h. Finally, the sea urchin-type $\text{Fe}_3\text{O}_4@\text{ZnO}$ hollow nanocomposites were separated with a magnet after repeatedly washing with deionized water and drying in a vacuum oven at 60 °C for 6 h.

Characterization and Measurements: The X-ray diffraction (XRD) patterns were recorded by a MAC Science MXP-18 X-ray diffractometer with a Cu target radiation source. The scanning electron microscopic (SEM) images were taken with a JEOL 7800F scanning electron microscope (operating at 5.0 kV). The transmission electron micrographs (TEM) and high-resolution transmission electron microscopy (HRTEM) images were taken with a JEM-2100 transmission electron microscope. Magnetic properties were measured by a Quantum Design MPMS3 superconducting quantum interference device (SQUID) magnetometer. The photoluminescence (PL) measurements were carried out on the Renishaw in via spectroscopy excited by a continuous He-Cd laser (wavelength: 325 nm and power: 2 mW). The UV-vis diffuse reflectance spectra (DRS) were obtained on a UV-5800PC.

Photocatalytic Performance Measurements: The W-FZ and the S-FZ structures were applied to degrade a model pollutant of rhodamine B (RhB),

respectively, and their photocatalytic performances were evaluated. The experiments were conducted at room temperature as follows: 50 mg of the as-prepared photocatalyst was added to the RhB solution (50 mL, 5 mg L⁻¹) and the mixture was mechanically stirred in the dark for 30 min to guarantee the adsorption–desorption equilibrium for RhB. Then, the mixture was exposed to UV irradiation from a 250 W high-pressure mercury lamp with average light intensity of 22.11 mW cm⁻² (centered at 365 nm). At given intervals of illumination, the concentration of RhB was analyzed by a UV–Vis spectrophotometer (UV-5800PC, Shanghai Metash Instruments Co., Ltd) with 14 cm away between the cuvettes and the light source, and then the percentage degradation was calculated.

Supporting Information

Supporting Information is available from the Wiley Online Library or from the author.

Acknowledgements

S.J. and M.P. contributed equally to this work. The National Key Research and Development Program of China (grant no. 2017YFF0108600). The authors acknowledge financial support from the Program for the Development of Science and Technology of Jilin Province (item nos. 20200201022JC, 20200801055GH, and 20200201023JC), the Thirteenth Five-Year Program for Science and Technology of Education Department of Jilin Province (grant no. JJKH20210611KJ), the National Youth Program Foundation of China (61805233), and the Program of Jilin Provincial Development and Reform Commission (grant no. 2021C036-3).

Conflict of Interest

The authors declare no conflict of interest.

Data Availability Statement

Research data are not shared.

Keywords

hollow core–shell heterostructures, magnetic responses, photocatalysis, recyclability

Received: June 30, 2021

Revised: August 14, 2021

Published online:

- [1] J. Kosco, M. Bidwell, H. Cha, T. Martin, C. T. Howells, M. Sachs, D. H. Anjum, S. Gonzalez Lopez, L. Zou, A. Wadsworth, W. Zhang, L. Zhang, J. Tellam, R. Sougrat, F. Laquai, D. M. DeLongchamp, J. R. Durrant, I. McCulloch, *Nat. Mater.* **2020**, 19, 559.
- [2] A. Serra, L. Philippe, *Chem. Eng. J.* **2020**, 401, 126164.
- [3] D. D. Wang, D. L. Han, Z. Shi, J. Wang, J. H. Yang, X. Y. Li, H. Song, *Appl. Catal., B* **2018**, 227, 61.
- [4] D. L. Han, B. X. Li, S. Yang, X. Y. Wang, W. Gao, Z. J. Si, Q. H. Zuo, Y. H. Li, Y. W. Li, Q. Duan, D. D. Wang, *Nanomaterials* **2019**, 9, 16.
- [5] X. C. Ma, Y. Dai, L. Yu, B. B. Huang, *Light Sci. Appl.* **2016**, 5, 16017.
- [6] S. S. Chen, T. Takata, K. Domen, *Nat. Rev. Mater.* **2017**, 2, 17050.
- [7] F. Pincella, K. Isozaki, K. Miki, *Light Sci. Appl.* **2014**, 3, 133.
- [8] J. X. Low, J. G. Yu, M. Jaroniec, S. Wageh, A. A. Al-Ghamdi, *Adv. Mater.* **2017**, 29, 1601694.
- [9] K. Acuña, J. Yáñez, S. Ranganathan, E. Ramírez, J. Pablo Cuevas, H. D. Mansilla, P. Santander, *Sol. Energy* **2017**, 157, 335.
- [10] V. Gilja, K. Novaković, J. Trivas-Sejdic, Z. Hrnjak-Murčić, M. Kraljić Roković, M. Žic, *Nanomaterials* **2017**, 7, 412.
- [11] M. Kaur, C. M. Nagaraja, *Mater. Lett.* **2015**, 154, 90.
- [12] H. Yang, Z. Jin, K. Fan, D. Liu, G. Lu, *Superlattices Microstruct.* **2017**, 111, 687.
- [13] Y. Wang, W. Jiang, W. Luo, X. Chen, Y. Zhu, *Appl. Catal., B* **2018**, 237, 633.
- [14] B. Lu, S. Zeng, C. Li, Y. Wang, X. Pan, L. Zhang, H. Mao, Y. Lu, Z. Ye, *Carbon* **2018**, 132, 191.
- [15] X. Guo, H. J. Zhu, Q. Li, *Appl. Catal., B* **2014**, 160–161, 408.
- [16] A. B. Djurisić, X. Y. Chen, Y. H. Leung, A. M. C. Ng, *J. Mater. Chem.* **2012**, 22, 6526.
- [17] L. H. Yu, W. Chen, D. Z. Li, J. B. Wang, Y. Shao, M. He, P. Wang, X. Z. Zheng, *Appl. Catal., B* **2015**, 164, 453.
- [18] S. Yang, J. C. Yao, Y. N. Quan, M. Y. Hu, R. Su, M. Gao, D. L. Han, J. H. Yang, *Light Sci. Appl.* **2020**, 9, 117.
- [19] X. Wang, Y. Ding, C. J. Summers, Z. L. Wang, *J. Phys. Chem. B* **2004**, 108, 8773.
- [20] K. Yuan, F. Li, L. Chen, Y. F. Li, Y. W. Chen, *J. Phys. Chem. C* **2012**, 116, 6332.
- [21] W. He, H. Jia, J. Cai, X. Han, Z. Zheng, W. G. Warner, J.-J. Yin, *J. Phys. Chem. C* **2016**, 120, 3187.
- [22] H. H. Wang, P. J. Zhou, R. Guo, Y. F. Wang, H. J. Zhan, Y. F. Yuan, *Catalysts* **2018**, 8, 107.
- [23] V. L. Prasanna, R. Vijayaraghavan, *Langmuir* **2015**, 31, 9155.
- [24] J. F. Guo, B. W. Ma, A. Y. Yin, K. N. Fan, W. L. Dai, *Appl. Catal., B* **2011**, 101, 580.
- [25] M. Cano, K. Sbargoud, E. Allard, C. Larpent, *Green Chem.* **2012**, 14, 1786.
- [26] I. E. Medina-Ramirez, C. E. D. de Leon-Macias, G. Pedroza-Herrera, R. Gonzales-Segovia, J. A. Zapien, J. L. Rodriguez-Lopez, *Ceram. Int.* **2020**, 46, 8979.
- [27] M. G. Dazmiri, H. Alinezhad, Z. Hossaini, A. R. Bekhradnia, *Appl. Organomet. Chem.* **2020**, 34, 5731.
- [28] Y. F. Wang, J. Gao, Y. Liu, M. T. Li, M. Zhang, G. He, Z. Q. Sun, *Opt. Mater.* **2021**, 111, 110608.
- [29] J. Wang, J. H. Yang, X. Y. Li, D. D. Wang, B. Wei, H. Song, X. F. Li, S. W. Fu, *Phys. E* **2016**, 75, 66.
- [30] X. L. Zhao, J. D. Li, X. Y. Cui, Y. J. Bi, X. J. Han, *J. Environ. Chem. Eng.* **2020**, 8, 103548.
- [31] D. P. Sun, Q. Zou, Y. P. Wang, Y. J. Wang, W. Jiang, F. S. Li, *Nanoscale* **2014**, 6, 6557.
- [32] C. Karunakaran, P. Vinayagamorthy, *Langmuir* **2014**, 30, 15031.
- [33] R. Yousefi, F. Jamali-Sheini, M. Cheraghizade, S. Khosravi-Gandomani, A. Saaedi, N. M. Huang, W. J. Basirun, M. Azarang, *Mater. Sci. Semicond. Process.* **2015**, 32, 152.
- [34] C. D. Li, J. P. Lv, Z. Q. Liang, S. L. Yao, *Opt. Mater.* **2013**, 35, 586.
- [35] J. W. P. Hsu, D. R. Tallant, R. L. Simpson, N. A. Missert, R. G. Copeland, *Appl. Phys. Lett.* **2006**, 88, 252103.
- [36] H. Usui, *J. Phys. Chem. C* **2007**, 111, 9060.
- [37] W. M. Kwok, A. B. Djurišić, Y. H. Leung, W. K. Chan, D. L. Phillips, *Appl. Phys. Lett.* **2005**, 87, 223111.
- [38] Z. Ambrus, N. Balázs, T. Alapi, G. Wittmann, P. Sipos, A. Dombi, K. Mogyorósi, *Appl. Catal., B* **2008**, 81, 27.
- [39] J. Wang, J. Yang, X. Li, D. Wang, B. Wei, H. Song, X. Li, S. Fu, *Phys. E* **2016**, 75, 66.
- [40] S. Abramson, L. Srithammavanh, J.-M. Siaugue, O. Horner, X. Xu, V. Cabuil, *J. Nanopart. Res.* **2009**, 11, 459.

- [41] X. F. Bian, K. Q. Hong, X. Ge, R. Song, L. Q. Liu, M. X. Xu, *J. Phys. Chem. C* **2015**, 119, 1700.
- [42] A. B. Djurišić, W. C. H. Choy, V. A. L. Roy, Y. H. Leung, C. Y. Kwong, K. W. Cheah, T. K. Gundu Rao, W. K. Chan, H. Fei Lui, C. Surya, *Adv. Funct. Mater.* **2004**, 14, 856.
- [43] H. Y. Xu, M. W. Shao, T. Chen, S. J. Zhuo, C. Y. Wen, M. F. Peng, *Microporous Mesoporous Mater.* **2012**, 153, 35.
- [44] Z. Y. Fan, P. C. Chang, J. G. Lu, E. C. Walter, R. M. Penner, C. H. Lin, H. P. Lee, *Appl. Phys. Lett.* **2004**, 85, 6128.
- [45] T. Andelman, Y. Gong, M. Polking, M. Yin, I. Kuskovsky, G. Neumark, S. O'Brien, *J. Phys. Chem. B* **2005**, 109, 14314.
- [46] J. P. Wang, Z. Wang, B. B. Huang, *ACS Appl. Mater. Interface* **2012**, 4, 4024.
- [47] Y. F. Sun, J. H. Yang, L. L. Yang, M. Gao, X. N. Shan, Z. Q. Zhang, M. B. Wei, Y. Liu, L. H. Fei, H. Song, *J. Lumin.* **2013**, 134, 35.
- [48] T. Tachikawa, S. Yamashita, T. Majima, *Angew. Chem., Int. Ed.* **2010**, 49, 432.
- [49] L. Wu, Y. Wu, X. Pan, F. Kong, *Opt. Mater.* **2006**, 28, 418.
- [50] Y. Zheng, C. Chen, Y. Zhan, X. Lin, Q. Zheng, K. Wei, J. Zhu, Y. Zhu, *Inorg. Chem.* **2007**, 46, 6675.
- [51] J. Wang, P. Liu, X. Fu, Z. Li, W. Han, X. Wang, *Langmuir* **2009**, 25, 1218.
- [52] X. Q. Xu, B. X. Lin, L. J. Sun, Z. X. Fu, *J. Phys. D: Appl. Phys.* **2009**, 42, 085102.
- [53] P. Erhart, K. Albe, A. Klein, *Phys. Rev. B* **2006**, 73, 205203.
- [54] L. Xue, P. Zhou, C. X. Zhang, C. Y. He, G. L. Hao, L. Z. Sun, J. X. Zhong, *AIP Adv.* **2013**, 3, 0521051.
- [55] S. B. Atla, W. R. Lin, T. C. Chien, *Mater. Chem. Phys.* **2018**, 216, 380.
- [56] X. Liu, D. Xu, D. Zhang, G. Zhang, L. Zhang, *Appl. Catal., B* **2016**, 186, 193.
- [57] G. Xi, B. Yue, J. Cao, J. Ye, *Chemistry* **2011**, 17, 5145.